

On the improved performances of FLUKA v4-4.0 in out-of-field proton dosimetry

Alexandra-Gabriela Șerban^{a,b,c}, Juan Alejandro de la Torre González^{d,e},
Marta Anguiano^{d,e}, Antonio M. Lallena^{d,e}, Francesc Salvat-Pujol^{a,*}

^aEuropean Organization for Nuclear Research, Esplanade des Particules 1, 1211 Geneva 23, Switzerland

^bFaculty of Physics, University of Bucharest, 405 Atomistilor, 077125 Bucharest-Magurele, Romania

^c“Horia Hulubei” National Institute of Physics and Nuclear Engineering, 30 Reactorului,
077125 Bucharest-Magurele, Romania

^dDepartamento de Física Atómica, Molecular y Nuclear, Universidad de Granada, E-18071, Granada, Spain

^eInstituto de Investigación Biosanitaria (ibs.GRANADA),

Complejo Hospitalario Universitario de Granada/Universidad de Granada, E-18016, Granada, Spain

Abstract

A new model for the nuclear elastic scattering of protons below 250 MeV has been recently included in FLUKA v4-4.0, motivated by the evaluation of radiation effects in electronics. Nonetheless, proton nuclear elastic scattering plays a significant role also in proton dosimetry applications, for which the new model necessitated an explicit validation. Therefore, in this work a benchmark has been carried out against a recent measurement of radial-depth maps of absorbed dose in a water phantom under irradiation with protons of 100 MeV, 160 MeV, and 225 MeV. Two FLUKA versions have been employed to simulate these dose maps: v4-3.4, relying on a legacy model for proton nuclear elastic scattering, and v4-4.0, relying on the new model. The enhanced agreement with experimental absorbed doses obtained with FLUKA v4-4.0 is discussed, and the role played by proton nuclear elastic scattering, among other interaction mechanisms, in various regions of the radial-depth dose map is elucidated. Finally, the benchmark reported in this work is sensitive enough to showcase the importance of accurately characterizing beam parameters and the scattering geometry for Monte Carlo simulation purposes.

Keywords: Monte Carlo, FLUKA, proton nuclear elastic scattering, radial-depth dose map, proton dosimetry.

1. Introduction

FLUKA [1–3] is a general-purpose code for the Monte Carlo (MC) simulation of coupled hadronic and electromagnetic radiation showers in complex geometries. It can transport over 60 particles species with energies from the keV to the PeV domain, with neutrons exceptionally tracked down to 0.01 meV. Naturally, FLUKA is routinely employed in a wide variety of applications, ranging from accelerator design and operation [4], to associated radiation protection studies [5, 6], the assessment of radiation effects in electronics [7–9], and medical applications [10–12], to name but a few.

Recent studies assessing the production of single-event-upsets in electronic devices under proton irradiation revealed a significant FLUKA underestimation for proton energies between 1 and 10 MeV [13]. This shortcoming was attributed to a too simplistic model for the nuclear elastic scattering of protons up to FLUKA version v4-3.4 [14] (included). In FLUKA v4-4.0 (released on Feb. 14, 2024), a new model for the nuclear elastic scattering of protons from Coulomb barrier up to 250 MeV was included [15], relying on a partial-wave analysis of experimental angular distributions [16, 17]. This model significantly improved FLUKA’s capability to evaluate single-event-upset production in electronic devices under irradiation by protons with energies from 1 to 100 MeV [15, 18].

Nuclear elastic scattering of protons plays a sig-

*Corresponding author

Email address: `fluka.team@cern.ch` (Francesc Salvat-Pujol)

nificant role, not only for the assessment of radiation effects in electronics [15, 19, 20], but also in proton dosimetry [21]. Indeed, proton nuclear elastic scattering contributes to the angular spread of proton showers in matter, and therefore has a direct effect on depth-dose maps, especially out-of-field (and thus on the dose delivered to nearby healthy tissue). A wide range of benchmarks was carried out prior to the public release of FLUKA v4-4.0 to validate its new model for proton nuclear elastic scattering [15]. Among them, a dedicated FLUKA simulation of a recent measurement of radial-depth (r - z) maps of dose absorbed in a water phantom under proton irradiation [22] was performed.

The aim of this work, done on behalf of the FLUKA.CERN Collaboration, is twofold: on the one hand, to showcase the improved performances of FLUKA v4-4.0 with respect to v4-3.4 in capturing features across various regions of the aforementioned experimental r - z dose maps and, on the other hand, to emphasize the importance of accurately characterizing the radiation source and the scattering geometry for MC simulation purposes. In Section 2, the experimental setup used to measure the aforementioned r - z dose maps [22] is summarized. Next, in Section 3, the proton source adopted in the corresponding FLUKA simulations is explicitly detailed and the rest of the simulation setup (geometry and scoring) is documented. In Section 4, the agreement between experimental r - z dose maps and those simulated with FLUKA v4-3.4 and v4-4.0 is discussed, putting particular emphasis on the significant role played by proton nuclear elastic scattering in various regions of the r - z dose maps. In Section 5, the virtues and shortcomings of the Fermi-Eyges proton beam definition adopted in [22] are outlined, and a procedure is proposed to capture features of the angular distribution beyond the Gaussian core that the Fermi-Eyges theory focuses on. Finally, in Section 6, a summary and conclusions are provided. Additionally, a general overview of the role played by proton nuclear elastic scattering and other relevant interaction mechanisms in the r - z maps of absorbed dose in water under proton irradiation is provided in the Appendix.

2. Experimental radial-depth dose maps

In a recent work [22], detailed r - z maps of dose absorbed in a water phantom under irradiation with 100 MeV, 160 MeV, and 225 MeV protons were

reported. In this section, a summary of the experimental setup aspects necessary for the FLUKA simulations below is provided; further details are deferred to the original reference [22].

The aforementioned r - z maps of absorbed dose were measured with a two-dimensional array of 1020 ionization chambers arranged in a square grid and placed in a water phantom of 40 cm length. The diameter of each cylindrical chamber was 0.42 cm and the center of the considered proton beam coincided with the center of one ionization chamber, as further detailed in [22]. The reported uncertainties at each experimental point were 2.5% in the absorbed dose, ± 0.07 cm in depth, and ± 0.01 cm in the radial position. Moreover, the experimental r - z dose maps were not given in absolute units: they were normalized to the dose at 3 cm on the beam axis.

N.B.: For the 100 MeV proton beam, at the radial distance of 2.29 cm, the labels on the y axis are inaccurate in the original reference. Correct experimental absorbed doses have been provided directly by the authors of the original paper [22].

3. FLUKA simulation setup

In [22], the spatial profile and angular distribution of the proton beam at the entrance of the water phantom are characterized relying on the Fermi-Eyges theory [23–25]. In this approach, the probability density to find a proton at a position \mathbf{r} after a path length s is parametrized as:

$$\Phi(s; \mathbf{r}, \theta_x, \theta_y) = F(z; x, \theta_x)F(z; y, \theta_y), \quad (1)$$

where

$$F(z; x, \theta_x) = \frac{1}{4\pi\sqrt{B(z)}} \times \exp\left(-\frac{A_0(z)x^2 - 2A_1(z)x\theta_x + A_2(z)\theta_x^2}{4B(z)}\right) \quad (2)$$

is the probability density for a proton at depth z to have a transverse position x and an angle θ_x between the direction of motion projected on the xz plane and the z axis; similarly for the projections on the yz plane [24]. The beam parameters are the variance of the angular distribution ($2A_0$), the variance of the spatial distribution ($2A_2$), and their covariance ($2A_1$). The emittance of the proton beam is evaluated as $B = A_0A_2 - A_1^2$. Transverse

positions and angles are sampled following [22] as:

$$\begin{aligned} x &= \mu_x + \sqrt{2A_2}\xi_1 \\ \theta_x &= \mu_{\theta_x} + \sqrt{\frac{2A_1^2}{A_2}}\xi_1 + \sqrt{\frac{2B}{A_2}}\xi_2, \end{aligned} \quad (3)$$

where μ_x is the mean position, μ_{θ_x} is the mean angle, and $\xi_{1,2}$ are two normally distributed pseudo-random numbers; axial symmetry around the z -axis is assumed, therefore the same expressions with the same parameters hold for the y components. For completeness, the proton beam parameters at the entrance of the water phantom for 100 MeV, 160 MeV, and 225 MeV suggested by [22], are reported in Table 1.

Table 1: Fermi-Eyges proton beam parameters for 100 MeV, 160 MeV, and 225 MeV at the entrance of the water phantom [22].

	100 MeV	160 MeV	225 MeV
E (MeV)	100.150	160.244	225.142
σ_E (MeV)	0.614	0.835	0.513
$\sqrt{2A_2(0)}$ (cm)	0.536	0.334	0.320
$2A_1(0)$ (cm mrad)	1.320	0.809	0.773
$\sqrt{2A_0(0)}$ (mrad)	6.01	3.52	3.90
μ_x (cm)	0	0	0
μ_θ (mrad)	0	0	0

The FLUKA geometry adopted to simulate the r - z dose maps of [22], set up with the Flair graphical user interface [26, 27], is schematically represented in Fig. 1: a water cylinder of 35 cm length and 15 cm radius is aligned with the z axis, and a beam of protons is initiated at its entrance, employing the Fermi-Eyges theory of Eq. (1) to sample the initial position and direction of the primary protons. Three beam energies are considered in separate runs: 100 MeV, 160 MeV, and 225 MeV. In all cases, 2.5×10^8 primary protons are simulated.

Absorbed dose is scored in the water phantom as a function of depth at various radial distances from the beam axis for the three considered energies. For each radial distance, a cylindrical mesh scoring is employed to score the dose absorbed in the water phantom. A radial bin width of 0.42 cm is adopted, corresponding to the diameter of the ionization chamber used experimentally [22]. Table 2 summarizes the radial binning employed for

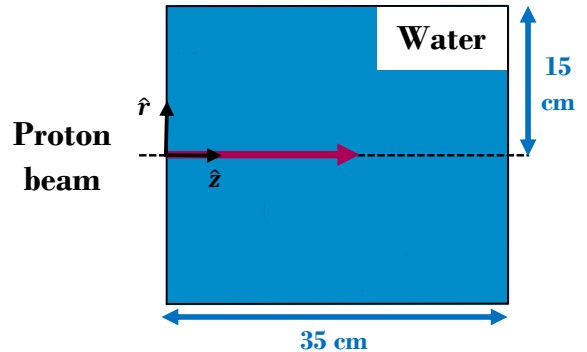


Figure 1: Schematic FLUKA simulation geometry showing the proton beam starting at the entrance of the water phantom.

the 100 MeV, 160 MeV, and 225 MeV proton beam cases, respectively. Following [22], a 1 mm bin width along the z axis is adopted.

Table 2: Radial binning employed in FLUKA to score the absorbed dose by 100 MeV, 160 MeV, and 225 MeV protons in water.

$r_j^{\min, \max}$ (cm)	100 MeV	160 MeV	225 MeV
r_1^{\min}	0.00	0.00	0.00
r_1^{\max}	0.42	0.42	0.42
r_2^{\min}	0.55	1.31	1.31
r_2^{\max}	0.97	1.73	1.73
r_3^{\min}	2.08	2.84	2.08
r_3^{\max}	2.50	3.26	2.50
r_4^{\min}	2.84	4.36	7.41
r_4^{\max}	3.26	4.78	7.83
r_5^{\min}	4.36	5.89	9.69
r_5^{\max}	4.78	6.31	10.11
r_6^{\min}	5.89	7.41	10.46
r_6^{\max}	6.31	7.83	10.88

Electron transport and production cut-offs in FLUKA are set to 50 keV. This choice, while slightly excessive (the range of 50 keV electrons in water is $\sim 43 \mu\text{m}$ [28, 29], much shorter than the adopted r and z resolutions), ensures that electron histories are stopped when they have practically no chance to contribute to any other r - z bin. Thus, the scored dose maps are free from particle-range-induced artefacts. For completeness, the produc-

tion and transport thresholds for photons are set to 100 eV, those for hadrons to 100 keV, neutrons are transported down to 0.01 meV, and light ions (d, t, ^3He , and ^4He) down to 100 keV; the production and transport thresholds for heavier ions are scaled from those of ^4He by the ratio of mass numbers. Furthermore, the mean excitation energy of water is set to $I=78$ eV [30].

4. FLUKA r - z dose maps

Employing the setup described in the foregoing section, the experimental r - z dose maps have been simulated with two FLUKA versions: v4-3.4, relying on the legacy model for proton nuclear elastic scattering [14], and v4-4.0 including a new model for this interaction mechanism [15]. Figure 2 displays r - z maps of absorbed dose in the water phantom for the 225 MeV proton beam case. Black dots represent the experimental absorbed dose of [22], while solid curves result from FLUKA v4-3.4 (blue) and v4-4.0 (green); dashed curves are discussed below. Dose maps are represented as a function of depth, but not integrated over the transverse plane; rather, the radial distance indicated in each panel is considered (see Table 2 for the used radial binnings). Doses are displayed in the arbitrary units adopted in [22], *i.e.*, normalized to the dose on-axis at $z = 3$ cm. At radial distances of $r = 0$ cm and $r = 1.52$ cm (panels 2a and 2b), where the dose is high, the remarkable agreement between the experimental dose and FLUKA v4-3.4 simulation results is retained in v4-4.0. At $r = 2.29$ cm (panel 2c), where the dose has already dropped by nearly two orders of magnitude, there is a slight improvement with FLUKA v4-4.0 at depths beyond 20 cm, where the dose is nevertheless sizeable. However, substantial improvement is obtained at $r = 7.62$ cm (panel 2d) at depths between 25 and 30 cm. At these depths, better agreement is also obtained at $r = 9.90$ cm and $r = 10.67$ cm (panels 2e and 2f), although slight discrepancies remain, which are discussed at the end of Section 5.

The same comparison is displayed in Fig. 3 for the 160 MeV proton beam case, with its corresponding radial binnings (see Table 2). FLUKA v4-4.0 simulation results at $r = 0$ cm, $r = 1.52$ cm, and $r = 4.57$ cm (panels 3a, 3b, and 3d) are slightly, yet noticeably, closer to the experimental absorbed dose than those of v4-3.4; for $r = 1.52$ cm (panel 3b), the considerable overestimation of the experimental absorbed dose in FLUKA v4-3.4

is only minimally reduced in v4-4.0. A similar disagreement with the experimental absorbed doses was found in [22], for simulations performed with other MC codes. Instead, at $r = 3.05$ cm (panel 3c), the agreement is substantially improved with FLUKA v4-4.0. However, at $r = 6.10$ cm and $r = 7.62$ cm (panels 3e and 3f), the differences between the experimental absorbed dose and FLUKA v4-3.4 estimates, which are further scrutinized below, are not improved with v4-4.0: the simulated absorbed doses remain much lower than the experimental dose. Moreover, the additional feature at depths between 15 and 20 cm is not captured at all, especially for $r = 7.62$ cm (see Section 5).

Lastly, Fig. 4 depicts the same benchmark for the 100 MeV proton beam case, with its corresponding radial binnings (see Table 2). The performances of FLUKA v4-3.4 and v4-4.0 are similar throughout all radial distances considered here. The agreement with experimental absorbed doses at $r = \{0, 0.76, 2.29\}$ cm (panels 4a, 4b, and 4c) is reasonable. Instead, at $r = \{3.05, 4.57, 6.10\}$ cm (panels 4d, 4e, and 4f) considerable discrepancies remain.

Before further investigating in Section 5 the origin of the shortcomings at $r = 6.10$ cm and $r = 7.62$ cm for the 160 MeV case and at $r = \{3.05, 4.57, 6.10\}$ cm for the 100 MeV case, the physical origin of the improvements observed with FLUKA v4-4.0 is substantiated. For this purpose, FLUKA's particle-latching capabilities have been exploited to disentangle the contribution of various kinds of particle histories to the r - z dose maps. For the three considered energies, Figs. 2, 3, and 4 additionally depict the contribution to the total absorbed dose from particle histories where protons underwent a nuclear elastic scattering event on oxygen in FLUKA v4-3.4 (dashed blue curve) and in v4-4.0 (dashed green curve), respectively. The magnitude of the dashed curves confirms that proton nuclear elastic scattering plays a dominant role at large radial distances. Even on axis it is seen to have a relevant contribution towards the end of the proton range. The significant increase in the FLUKA v4-4.0 dose, helping to narrow the gap with experimental absorbed doses at large radial distances and large depths for the 160 MeV and 225 MeV cases, indeed stems from a more accurate treatment of proton nuclear elastic scattering in FLUKA v4-4.0. In particular, nuclear elastic scattering events of protons on oxygen are described more accurately, since the FLUKA v4-4.0 model

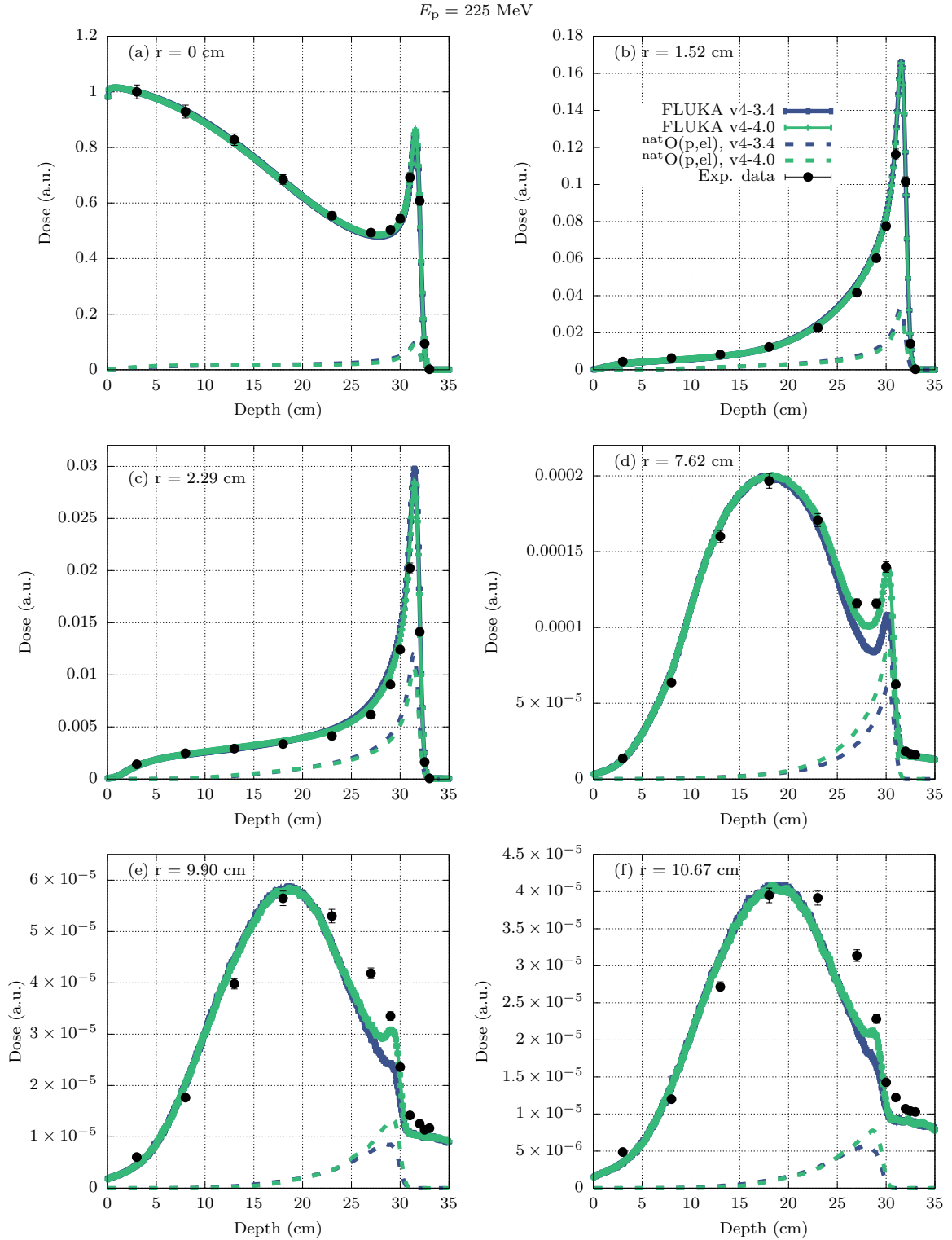


Figure 2: Absorbed dose in arbitrary units as a function of depth by 225 MeV protons in water scored with FLUKA v4-3.4 (solid blue) and v4-4.0 (solid green) at the various indicated radial distances. The black dots represent experimental absorbed doses [22]. The blue and green dashed curves show the contribution from particle histories where protons underwent a nuclear elastic scattering event on oxygen, scored with FLUKA v4-3.4 and v4-4.0, respectively.

$E_p = 160 \text{ MeV}$

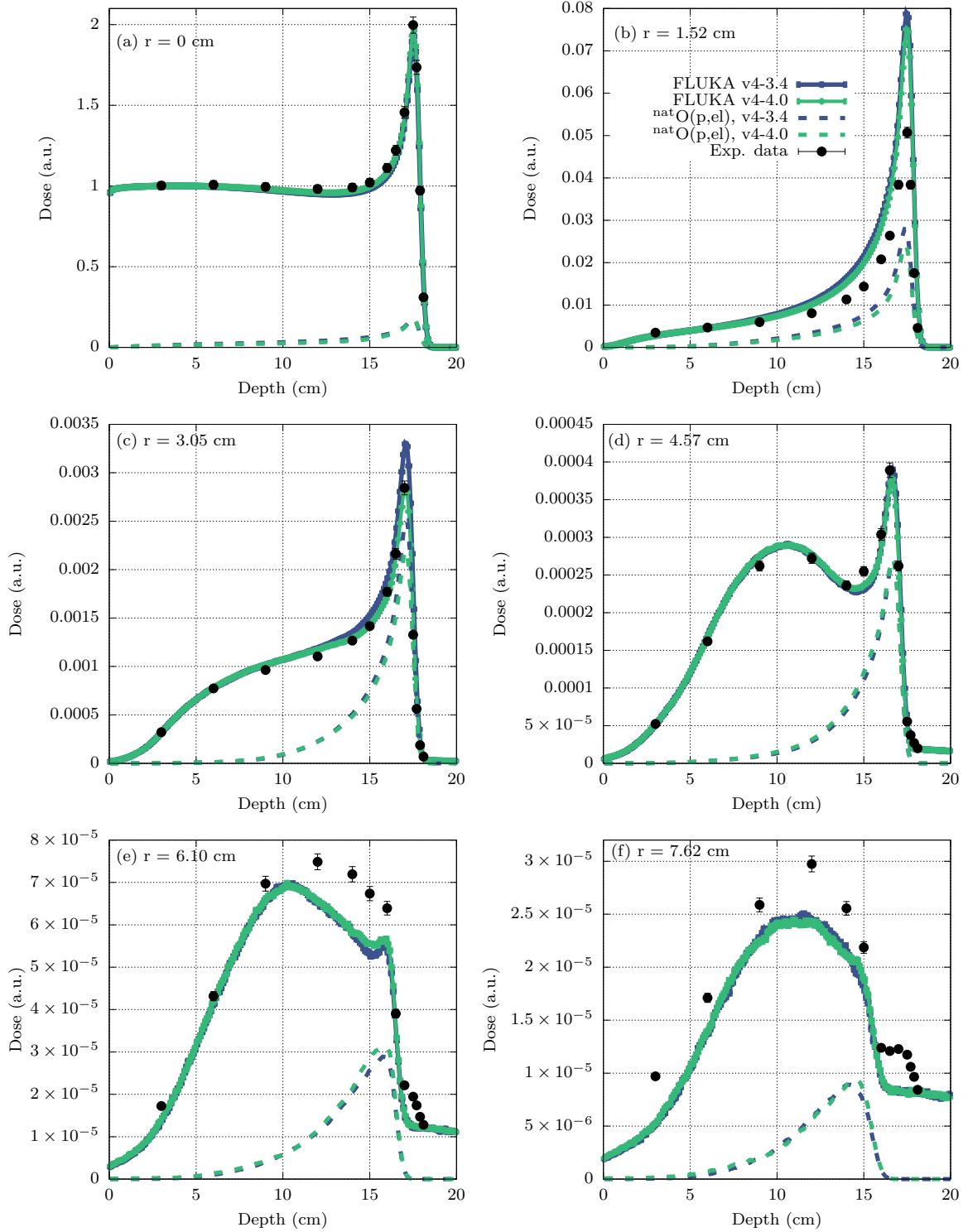


Figure 3: Same as Fig. 2 for 160 MeV protons.

$E_p = 100$ MeV

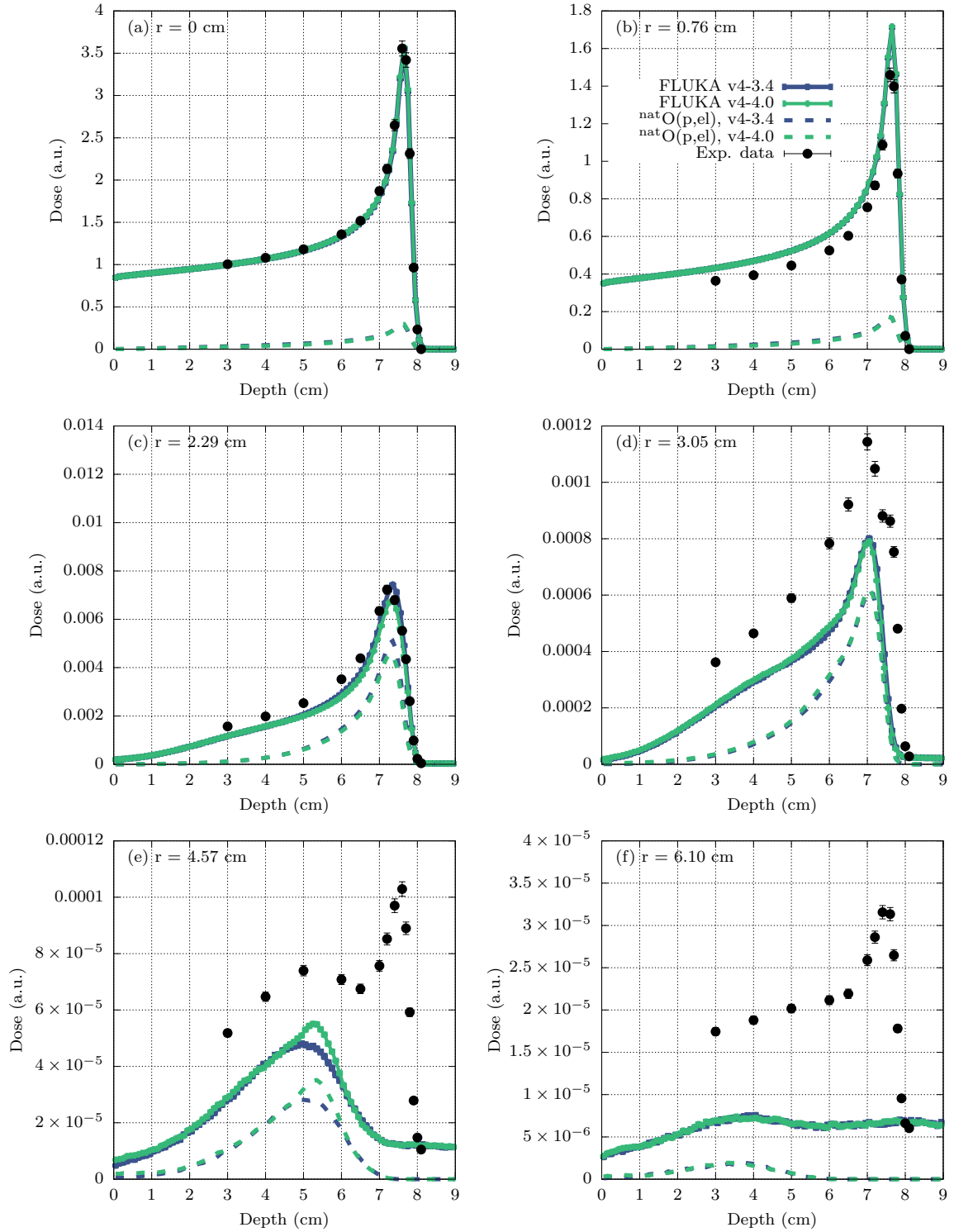


Figure 4: Same as Fig. 2 for 100 MeV protons.

relies on a fit to experimental differential cross sections for light nuclei [16, 17]. For the 100 MeV proton beam case, a similar behaviour is found.

Table 3: Relative root mean square deviation, Eq. (4), of the absorbed dose in water under 100 MeV, 160 MeV, and 225 MeV proton irradiation, simulated with FLUKA v4-3.4 and FLUKA v4-4.0.

E (MeV)	r_j (cm)	$\delta(r_j)$	
		FLUKA v4-3.4	FLUKA v4-4.0
100	0	0.0274	0.0258
	0.76	0.0805	0.0823
	2.29	0.0544	0.0738
	3.05	0.3200	0.3299
	4.57	0.5639	0.5617
	6.10	0.6209	0.6196
160	0	0.0304	0.0269
	1.52	0.2938	0.2598
	3.05	0.0862	0.0327
	4.57	0.0332	0.0293
	6.10	0.1231	0.1128
	7.62	0.1652	0.1663
225	0	0.0153	0.0119
	1.52	0.0360	0.0332
	2.29	0.0726	0.0504
	7.62	0.0834	0.0296
	9.90	0.1098	0.0813
	10.67	0.1214	0.1029

To quantify the agreement between doses simulated with FLUKA v4-3.4/v4-4.0 and the experimental absorbed dose at each radial distance, the relative root mean square deviation is adopted:

$$\delta(r_j) = \frac{\sqrt{\frac{1}{N} \sum_{i=1}^N (D_{ij}^{\text{FLUKA}} - D_{ij}^{\text{exp}})^2}}{D_j^{\text{exp,max}} - D_j^{\text{exp,min}}}, \quad (4)$$

where N is the number of experimental points along the z axis at each radial distance r_j , $j = \{1, 2, 3, 4, 5, 6\}$, while D_{ij}^{FLUKA} and D_{ij}^{exp} are the FLUKA-simulated and the experimental absorbed dose at each z_i and r_j , respectively. The maximum and minimum experimental absorbed dose at each r_j are denoted by $D_j^{\text{exp,max}}$ and $D_j^{\text{exp,min}}$, respectively. Table 3 displays $\delta(r_j)$ evaluated for both FLUKA v4-3.4 and v4-4.0. For the 225 MeV proton beam case, $\delta(r_j)$ confirms that better agreement with the experimental absorbed dose is achieved

at all radial distances with FLUKA v4-4.0 than with v4-3.4. Likewise for the 160 MeV proton beam case, except for $r = 7.62$ cm, where $\delta(r_j)$ are comparable for both versions of the code. For the 100 MeV case, both FLUKA versions have similar $\delta(r_j)$.

5. Source term for the 100 MeV and 160 MeV proton beams

As shown in Section 4, the Fermi-Eyges description of the proton beam at the entrance of the water phantom is sufficiently effective for the purposes of the MC simulation of the experimental r - z dose maps [22] for protons of 225 MeV, at all radial distances considered here, as well as for protons of 160 MeV and 100 MeV, but only on axis. Instead, at large radial distances, several underestimations and missing features are witnessed for the latter two proton energies. Similar difficulties were reported in [22]. In this section, the underlying issues are substantiated and an effective prescription to overcome them is proposed.

The Fermi-Eyges theory outlined in Section 3 is effective at capturing the dominating Gaussian core of the angular distribution of protons impinging on the water phantom, stemming from multiple Coulomb scattering (MCS) as the incoming protons traverse air on their path from the beamline to the water phantom. However, it does not account for large-scattering-angle contributions (be it from Coulomb or nuclear elastic scattering) extending to angles beyond those of the Gaussian core. To elucidate this point in a simplified way, Fig. 5 displays angular distributions of 225 MeV (yellow circles), 160 MeV (green squares), and 100 MeV (purple diamonds) proton pencil beams after traversing 50 cm of air, sampled with FLUKA. These curves indeed exhibit a dominating Gaussian structure around the incoming direction, but also the expected larger-scattering-angle tail. The solid curves of matching colours display the extent to which a Gaussian fit manages to reproduce these angular distributions. This analysis suggests that the Fermi-Eyges source model is not sufficiently accurate to capture large- r features for the 160 MeV and 100 MeV cases, hence the difficulties reported in Figs. 3 and 4.

To explicitly simulate deflections beyond the Fermi-Eyges Gaussian core, an air layer has been added in front of the water phantom, as depicted in Fig. 6, in which protons may undergo nuclear elastic scattering. The proton source must therefore be

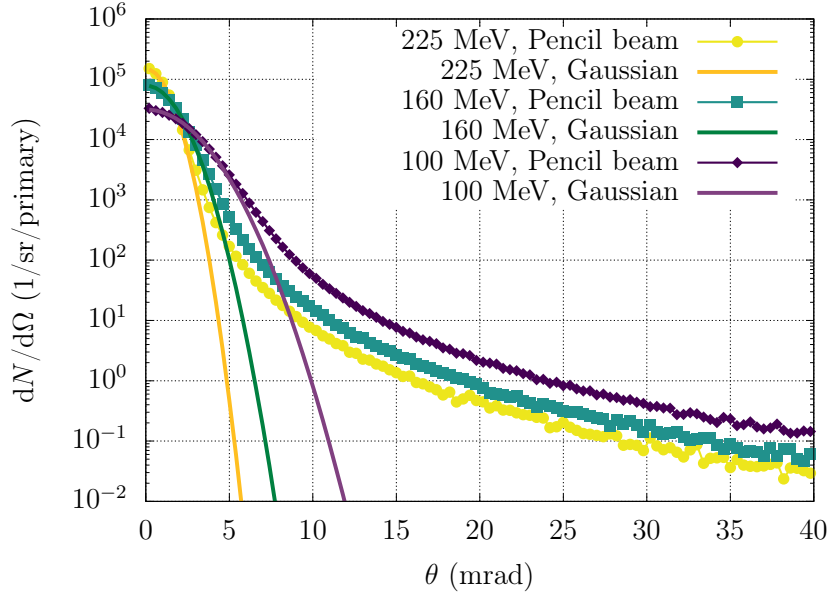


Figure 5: Comparison between FLUKA sampled angular distributions of pencil proton beams after 50 cm of air vs. fitted Gaussian distributions for proton energies of 225 MeV (yellow circles), 160 MeV (green squares), and 100 MeV (purple diamonds).

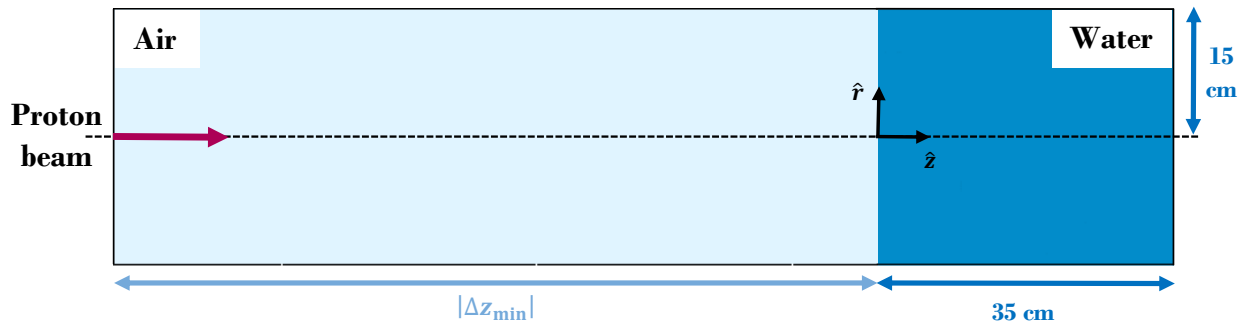


Figure 6: Schematic FLUKA simulation setup for the 100 MeV and 160 MeV proton beams, consisting of the water phantom and the impinging proton beam after traversing an air layer.

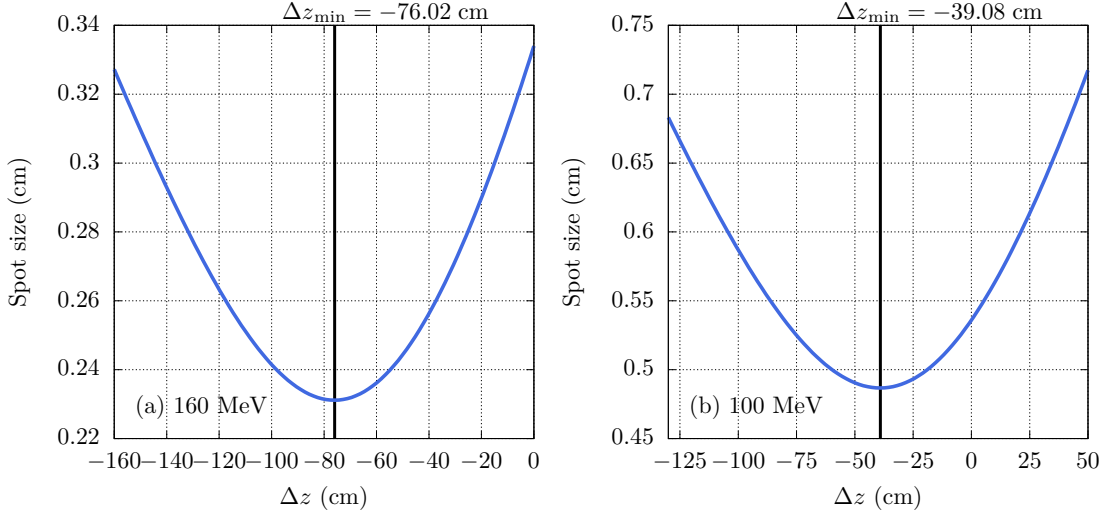


Figure 7: Beam spot size as a function of source displacement.

retracted and the corresponding Fermi-Eyges beam parameters must be determined. Since these are known at the entrance of the water phantom [22], the new beam parameters can be determined following [25], assuming that air is a weak scatterer, as:

$$\begin{aligned}
 A_0(z) &= A_0(z_1) + T\Delta z \\
 A_1(z) &= A_1(z_1) + A_0(z_1)\Delta z + T\frac{\Delta z^2}{2} \\
 A_2(z) &= A_2(z_1) + 2A_1(z_1)\Delta z + \\
 &\quad + A_0(z_1)\Delta z^2 + T\frac{\Delta z^3}{3},
 \end{aligned} \tag{5}$$

where $\Delta z = z - z_1$; z_1 is the initial position of the source at the entrance of the water phantom, *i.e.*, 0 cm, and $z < 0$ is the new position of the source. The beam parameters at the entrance of the water phantom [22], *i.e.*, $A_0(z_1)$, $A_1(z_1)$, and $A_2(z_1)$, are summarized in Table 1. The scattering power [25]

$$T = \frac{d\langle\theta^2\rangle}{dz}, \tag{6}$$

assumed constant for air, has been estimated as follows. The angular distributions of 100 MeV and 160 MeV protons traversing air slabs of various thicknesses have been scored with FLUKA. The mean squared projected MCS angle has been evaluated for each considered thickness and T has been estimated using a finite difference approximation of Eq. (6). The beam spot size is:

$$\sigma_x(z) = \sqrt{2A_2(z)}. \tag{7}$$

Figure 7 displays the beam spot size as a function of the source displacement Δz for the 160 MeV (a) and 100 MeV (b) proton beam cases, respectively. The beam spot sizes attain a minimum at $\Delta z_{\min} = z_{\min} - z_1 = -76.02$ cm for 160 MeV and -39.08 cm for 100 MeV, indicated by the black vertical lines in Figs. 7a and 7b. The parameters of the retracted proton beams at the position of the minima are listed in Table 4. Beyond these minima, the Fermi-Eyges theory cannot be used to move the source farther back since this prescription only accounts for the beam spread [31], and not for beam focusing effects. Nevertheless, one can account for air layers thicker than $|\Delta z_{\min}|$ by scaling the density of an air layer of thickness $|\Delta z_{\min}|$ as

$$\rho_{\text{equiv}} = \rho_{\text{air}} \frac{|\Delta z|}{|\Delta z_{\min}|}, \tag{8}$$

where $\rho_{\text{air}} = 1.20479 \times 10^{-3}$ g/cm³ [32, 33] is the density of dry air at sea level and $|\Delta z| > |\Delta z_{\min}|$ is the thickness for which best agreement between simulated and experimental r - z dose maps is obtained (found by iteration). In this way, an air layer thicker than $|\Delta z_{\min}|$ can be effectively simulated without retracting the spatial position of the source beyond the domain of applicability of the Fermi-Eyges prescription. Due to the source displacement, the simulated proton beam loses energy in the additional air layer. Thus, the position of the Bragg peak changes. To obtain it at the correct depth, the beam energy is effectively adjusted

Table 4: Parameters of the retracted source at the position at which the beam spot size minimum is attained for the 100 MeV and 160 MeV proton beams.

	100 MeV	160 MeV
T (rad ² /cm)	12×10^{-8}	4.8×10^{-8}
Δz_{\min} (cm)	-39.08	-76.02
$\sqrt{2A_2(z_{\min})}$ (cm)	0.484	0.216
$2A_1(z_{\min})$ (cm mrad)	0.0916	0.133
$\sqrt{2A_0(z_{\min})}$ (mrad)	5.17	2.32

Table 5: Adjusted proton beam energy E' , thickness $|\Delta z|$ of the air layer, and equivalent density as per Eq. (8) employed for the 100 MeV and 160 MeV cases.

	100 MeV	160 MeV
E' (MeV)	101.167	161.450
$ \Delta z $ (cm)	130	220
ρ_{equiv} (g/cm ³)	4.00755×10^{-3}	3.48663×10^{-3}

as [34]:

$$E' = \left(E^p - \frac{\Delta z}{\alpha} \right)^{1/p}, \quad (9)$$

where E is the beam energy at the water phantom entrance, while $p = 1.7589$ and $\alpha = 2.194 \text{ MeV}^{-p} \text{ cm}$ are parameters obtained by fitting the energy-range power law $R = \alpha E^p$, where R is the range of protons in air [28, 35]. Additionally, since the straggling in air is negligible, the energy spread σ_E of the proton beam at the entrance of the water phantom, summarized in Table 1, remains unaltered. The adjusted proton beam energy E' , the equivalent air density ρ_{equiv} , and the thickness $|\Delta z|$ of the air layer needed to obtain ρ_{equiv} are outlined in Table 5.

Figures 8 and 9 show the drastic effect of the additional air layer in front of the water phantom for 160 MeV and 100 MeV, respectively, where it matters most, *i.e.*, at large radial distances from the beam axis. Experimental absorbed doses [22] are displayed in black symbols, while the FLUKA v4-4.0 estimates with and without the additional air layer are shown in yellow and green curves, respectively. The dashed magenta and blue

curves correspond to particle histories where protons underwent a nuclear elastic scattering in air, on nitrogen and on oxygen, respectively. These events occurring in the additional air layer prove to be essential: without their contribution (alongside the contribution from nuclear reactions of protons in air) the simulated dose is overall much lower than the experimental one. In particular, for 160 MeV the features exhibited by the experimental absorbed dose at $r = 6.10 \text{ cm}$ (panel 8e) and $r = 7.62 \text{ cm}$ (panel 8f) at depths around 15–20 cm are not captured at all by the simulated dose when the air layer is missing (green curves). Instead, with the latter properly accounted for, these additional features (originating from the nuclear elastic scattering of protons on nitrogen and on oxygen in air) are correctly reproduced (yellow curves). The agreement at the first four radial distances (panels 8a, 8b, 8c, 8d) has been generally preserved while retracting the source. The same holds for 100 MeV on axis (panel 9a) and at $r = 0.76 \text{ cm}$ (panel 9b). At $r = 2.29 \text{ cm}$ (panel 9c), there is a mild improvement which helps to close the gap between the FLUKA-simulated and the experimental absorbed dose. However, at $r = 3.05 \text{ cm}$ (panel 9d) and $r = 4.57 \text{ cm}$ (panel 9e) this is not the case: the increase in the FLUKA-simulated dose is insufficient to match the experimental absorbed dose (see below). The most remarkable enhancement, leading to a satisfactory agreement with the experimental absorbed dose, is seen at $r = 6.10 \text{ cm}$ (panel 9f). At this radial distance, proton nuclear elastic scattering on nitrogen in the air layer in front of the water phantom proves to have a massive contribution, as illustrated by the dashed magenta curve in panel 9f.

The mean free paths for the nuclear elastic scattering of 100 MeV, 160 MeV, and 225 MeV protons in air are $2.37 \times 10^4 \text{ cm}$, $6.75 \times 10^4 \text{ cm}$, and $2.34 \times 10^5 \text{ cm}$, respectively. While for protons of 100 MeV and 160 MeV the mean free paths are comparable, for 225 MeV protons it is one order of magnitude larger. This explains why the Fermi-Eyges source characterization was effective for the 225 MeV proton beam and not for 100 MeV and 160 MeV proton beams.

The features at $z = 0$ observed with the inclusion of the air layer in Figs. 8 and 9, notably at large r , are due to δ rays generated by secondary particles in the air region preceding the water phantom. These are travelling from a low-density medium (air) to a higher-density medium (water), where they have

$E_p = 160 \text{ MeV}$

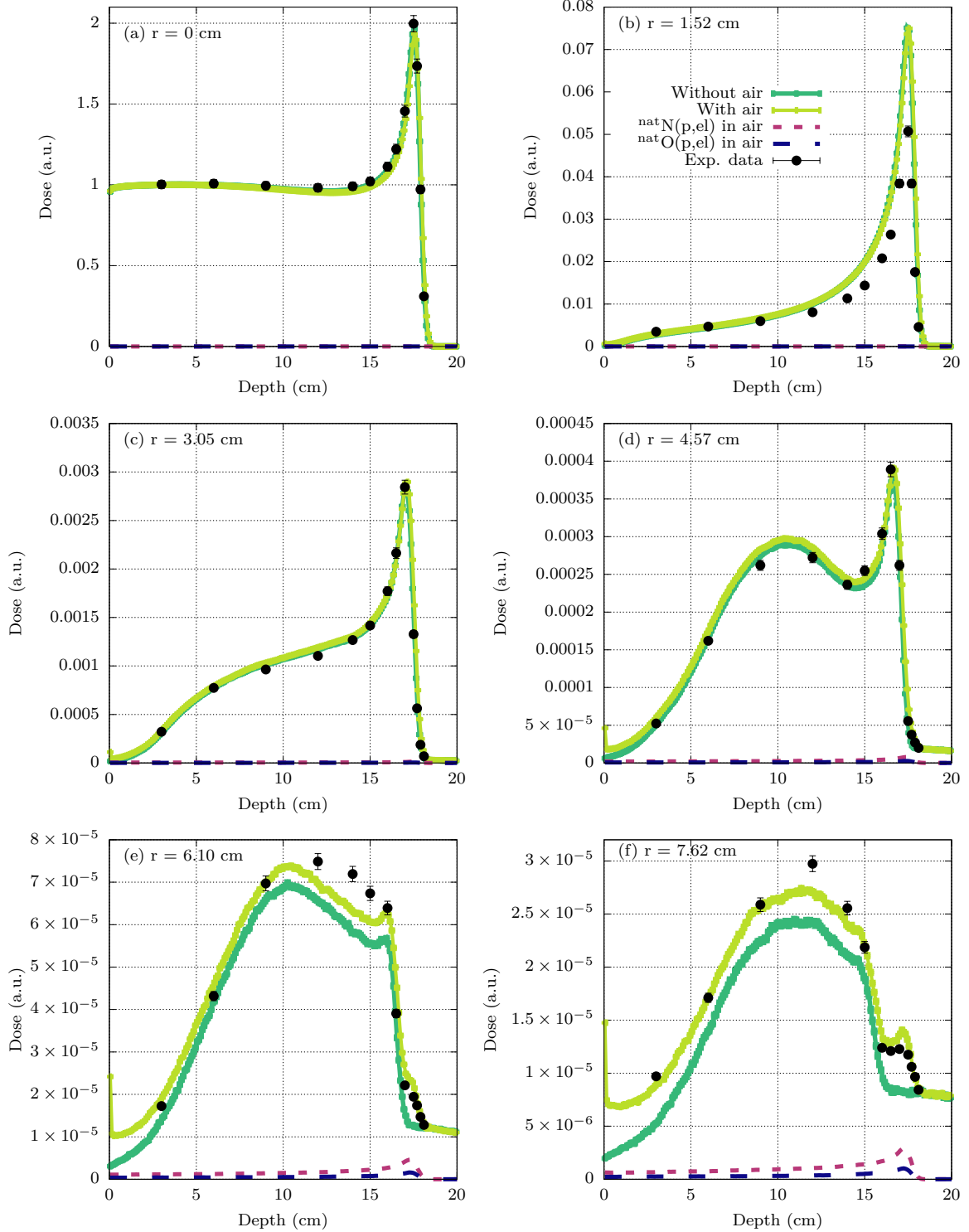


Figure 8: Absorbed dose in arbitrary units as a function of depth by 160 MeV protons in water scored with FLUKA v4-4.0 without (green) and with (yellow) the air layer. The black dots represent experimental absorbed doses [22]. The dashed curves correspond to contributions from particle histories where protons underwent a nuclear elastic scattering in air on nitrogen (magenta) and on oxygen (blue). In panels (a)-(c) these contributions nearly vanish at the scale of the figure.

$E_p = 100$ MeV

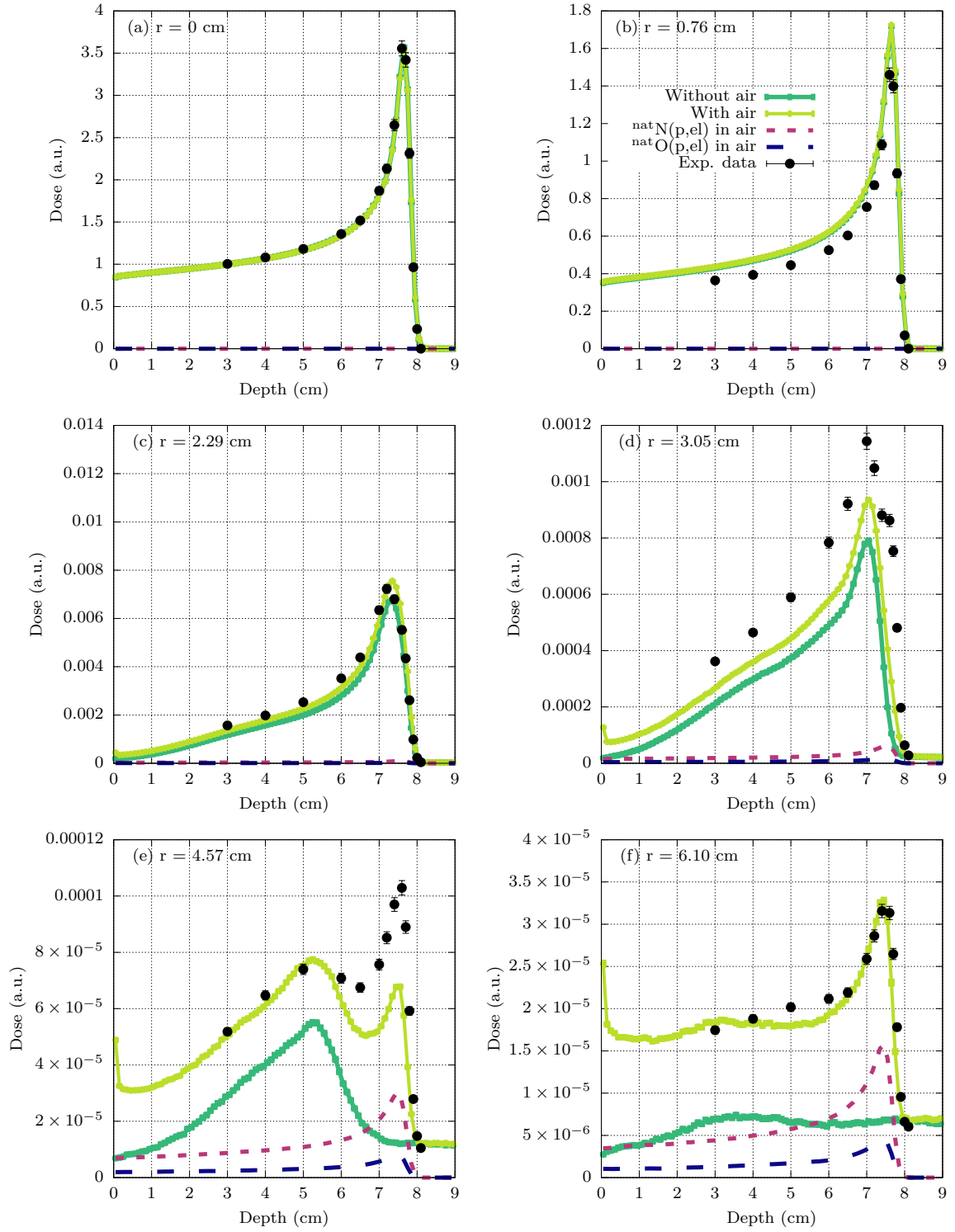


Figure 9: Same as Fig. 8 for 100 MeV.

a much shorter range. Thus, the δ rays generated in air deposit their energy over a shorter distance in water and lead to the observed localized dose deposition at the entrance of the phantom.

Table 6: Relative root mean square deviation, Eq. (4), of the absorbed dose in water under 100 MeV and 160 MeV proton irradiation, simulated with FLUKA v4-4.0 with and without the additional air layer.

E (MeV)	r_j (cm)	$\delta(r_j)$	
		Without air	With air
100	0	0.0258	0.0294
	0.76	0.0823	0.0890
	2.29	0.0738	0.0460
	3.05	0.3299	0.2301
	4.57	0.5617	0.2357
	6.10	0.6196	0.1163
160	0	0.0269	0.0616
	1.52	0.2598	0.2884
	3.05	0.0327	0.0718
	4.57	0.0293	0.0524
	6.10	0.1128	0.0625
	7.62	0.1663	0.0523

The adopted measure $\delta(r_j)$, Eq. (4), has been evaluated for the FLUKA v4-4.0 absorbed doses, taking into account the additional air layer in front of the water phantom and compared in Table 6 with the FLUKA v4-4.0 estimates from Table 3, where no air layer has been considered. While for the 160 MeV proton beam case, the agreement with the experimental absorbed dose at the first four radial distances is to a mild extent deteriorated by the addition of the air layer in front of the water phantom, at $r = 6.10$ cm and $r = 7.62$ cm there is substantial improvement due to the nuclear elastic and inelastic scattering of protons in air. Not only is the intensity in the simulated dose higher throughout the depth of the water phantom, but also the prominent features at depths beyond 15 cm are well reproduced. For the 100 MeV case, at $r = 0$ cm and $r = 0.76$ cm comparable $\delta(r_j)$ are obtained when considering or not the air layer since its effect on axis is negligible at this lower proton energy. Instead, at larger radial distances, better agreement with respect to the experimental absorbed dose is achieved. The most striking effect of the additional air layer in front of the water phantom is observed at $r = 6.10$ cm, stemming mainly from the nuclear elastic scattering of protons on nitrogen. At this radial distance,

the simulated dose increases substantially, matching the experimental absorbed dose.

Residual discrepancies between FLUKA v4-4.0-simulated and experimental absorbed doses remain for the last two radial distances of the 225 MeV case, as well as for the 160 MeV case (regardless of the additional air layer). Furthermore, for the 160 MeV case at $r = 1.52$ cm the considerable overestimation of the experimental absorbed dose by the simulated dose is obtained with both FLUKA versions, and it persists when the air layer is added in front of the water phantom. For the 100 MeV case, differences remain at $r = 3.05$ cm and $r = 4.57$ cm. Similar discrepancies as the aforementioned ones are reported also in the original study [22] for simulations performed with other MC codes. To investigate the extent to which nuclear interactions models could impact these discrepancies, the integrated cross section for both nuclear elastic and inelastic scattering of protons on oxygen in the energy range of interest (100–225 MeV) has been varied by a substantial $\pm 10\%$. This variation has been insufficient to close the gap between simulated and experimental absorbed doses (and, moreover, it compromised the good agreement at shallow depths). Therefore, the remaining differences may be due to uncertainties in the experimental absorbed doses, in the original Fermi-Eyges proton beam parameters (which propagate into uncertainties in source parameters in its retracted position at the entrance of the air layer), or due to simplifications of the actual experimental beamline layout for simulation purposes.

6. Conclusions

The recent inclusion of a new model for the nuclear elastic scattering of protons below 250 MeV in FLUKA v4-4.0 [15] implied a necessary reassessment of the code performance for proton dosimetry applications, for which this interaction mechanism plays a significant role. The absorbed r - z dose distributions reported in [22] constitute a valuable dataset against which to benchmark the performances of this new model. Thus, a detailed analysis of these r - z dose maps from 225 MeV, 160 MeV, and 100 MeV protons has been carried out both with FLUKA v4-3.4, relying on a legacy model for proton nuclear elastic scattering [14], and with v4-4.0, including the new model for this interaction mechanism.

For the 225 MeV proton beam case, this benchmark shows that, while on axis the excellent performances of FLUKA v4-3.4 are preserved, an enhanced agreement with the experimental absorbed dose is obtained out-of-field with v4-4.0. An explicit filtering of particle histories contributing to the total simulated dose confirms that these notable improvements result from a more accurate description of proton nuclear elastic scattering on oxygen, since the new model [15] relies on a fit to experimental differential cross sections [16, 17] for protons on light nuclei.

For the 160 MeV and 100 MeV proton beam cases, the new proton nuclear elastic scattering model leads to improvements which are, however, insufficient to reproduce the experimental absorbed dose, especially at large radial distances. For these two energies, the remaining notable discrepancies are instead due to an incomplete characterization of the proton source based on the Fermi-Eyges theory. The latter assumes a Gaussian approximation of the spatial and angular beam profiles, disregarding the large-angle contribution stemming from nuclear elastic scattering, which has a more significant impact the lower the proton energy. These shortcomings can be overcome by retracting the source and interspersing a layer of air in front of the water phantom to explicitly account for large-angle deflections. It has been shown in this work that a proper account of nuclear elastic scattering of protons on nitrogen and oxygen in the air layer is indispensable to capture the large- r features exhibited by the r - z dose maps of 160 MeV and 100 MeV protons.

FLUKA's excellent description of dose deposition has not only been preserved on axis, but substantial improvements have been achieved out-of-field thanks to the new model for proton nuclear elastic scattering implemented in FLUKA v4-4.0 [15]. Finally, the importance of an accurate definition of the radiation source term, in addition to the need of robust physics models, for detailed Monte Carlo simulation purposes has been highlighted.

Acknowledgements

The authors would like to express their gratitude to L. Brualla for generously providing the experimental radial-depth dose maps essential for this work. J.A. de la Torre González, M. Anguiano, and A.M. Lallena acknowledge that this work has been partially supported by the Spanish Ministerio

de Ciencia y Competitividad (PID2019-104888GB-I00, PID2022-137543NB-I00) and the European Regional Development Fund (ERDF).

Appendix

To illustrate how various interaction mechanisms contribute to dose absorption in the setup considered in this work, the particle-latching capabilities of FLUKA have been employed to explicitly score the contribution of different kinds of particle histories to various regions of the considered r - z dose maps. Figures 10, 11, and 12 respectively depict for 225 MeV, 160 MeV, and 100 MeV (the latter two with an additional air layer in front of the water phantom, as described in Section 5) the total dose scored with FLUKA v4-4.0 (teal). The total dose has been further resolved into the contributions from particle histories where protons have undergone a nuclear reaction (purple), from which the contribution resulting from neutron interactions (orange) has been explicitly filtered, nuclear elastic scattering on hydrogen (yellow), nuclear elastic scattering on oxygen (blue), nuclear elastic scattering on nitrogen (magenta), or no nuclear interactions. In all cases, the contribution of Coulomb scattering and ionization remains active.

For all considered energies, the dominant contribution on axis throughout the depth of the water phantom stems from particle histories where there were no nuclear interactions (green), as expected; this contribution diminishes with increasing radial distances from the beam axis. Conversely, the secondaries generated from nuclear reactions of protons (purple) have a high contribution at large radial distances and at intermediate depths. Among these secondaries, neutrons (and the particles resulting from their nuclear interaction) give rise to the plateau of the purple curves at large depths. Interestingly, there are some particular radial distances where the contribution of nuclear elastic scattering of protons on hydrogen (yellow), unaltered in FLUKA v4-4.0 with respect to v4-3.4, becomes significant, such as at $r = 7.62$ cm for 225 MeV, and at $r = 3.05$ cm and $r = 4.57$ cm for 160 MeV. The contribution of nuclear elastic scattering of protons on oxygen (blue) plays an important role both on axis and out-of-field for all three energies, especially at large depths. Lastly, for 160 MeV and 100 MeV, a surprisingly important role is played by the nuclear elastic scattering

of protons on nitrogen (magenta) in the additional air layer in front of the water phantom.

To further quantify the role played by each interaction mechanism in the r - z dose maps, the ratio $D_i(r, z)/D(r, z)$ has been evaluated, where $D_i(r, z)$ is the absorbed dose due to particle histories having undergone an event of kind $i = \{\text{no nuclear interactions, nuclear elastic scattering, nuclear reactions, neutron interactions}\}$ and $D(r, z)$ is the total absorbed dose. Figures 13, 14, and 15 display this ratio as a function of both the radial distance from the beam axis and the depth inside the water phantom; 10.5×10^9 primary protons have been simulated for these 2D maps. The contribution of proton histories which underwent no nuclear interactions, depicted in the upper left panels of the aforementioned figures, exhibits a higher dose ratio near the beam axis, promptly diminishing beyond the position of the Bragg peak, around 30-35 cm for 225 MeV protons, 15-20 cm for the 160 MeV protons, and 8-9 cm for the 100 MeV protons. As expected, the radial spread (driven by multiple Coulomb scattering) of this contribution is relatively narrow, with a significant contribution concentrated close to the beam axis that broadens at the end of the proton range. The maximum energy transfer from 100 MeV, 160 MeV, and 225 MeV protons to delta rays is of 229.19 keV, 377.79 keV, and 548.19 keV, respectively. At these energies, electrons can emit Bremsstrahlung photons, which can travel farther from the beam axis, thus explaining the non-zero dose ratio at large radial distances at all depths, even beyond the Bragg peak. Moreover, the particle tracks observed in the upper left panels for the 100 MeV and 160 MeV proton beam cases are due to secondary electrons emitted by these Bremsstrahlung photons via Compton scattering or the photoelectric effect.

The contribution of histories where nuclear elastic scattering occurred, displayed in the upper right panels, has a broader radial spread than that of histories where no nuclear interactions occurred for all three energies, since the differential cross section for proton nuclear elastic scattering is broader than that for Coulomb scattering [15]. Moreover, even if histories where nuclear elastic scattering occurred contribute to the overall dose less than those where no nuclear interactions occurred, this interaction mechanism plays a significant role at greater depths for all radial distances.

The contribution of histories where protons underwent nuclear reactions, depicted in the bottom

left panels, extends over a wide radial and depth range. Their contribution becomes more significant at greater radial distances compared to the contribution of histories where no nuclear interactions or nuclear elastic scattering events occurred. This is due to the production of secondary particles that can travel farther from the primary beam path. In particular, the contribution of histories where neutrons were produced, shown in the bottom right panels, is generally small, but it increases at larger depths for all radial distances. In water, neutrons abundantly undergo elastic scattering, which decreases their energy until they thermalize. These thermal neutrons have a high capture cross section and lead to the emission of \sim MeV photons, which can travel $\mathcal{O}(10)$ cm inside the water phantom, populating the large depths.

The contribution of histories where nuclear elastic scattering of protons occurred has been further split according to the target nucleus: oxygen or hydrogen. Figure 16 displays these two contributions on the left and right panels, respectively, for the 225 MeV, 160 MeV, and 100 MeV proton beams. In the course of a proton-hydrogen nuclear elastic scattering event, due to their equal masses, a larger momentum transfer might occur than in proton-oxygen elastic scattering. This large momentum transfer explains the broader radial extent of the absorbed dose in the case of a proton nuclear elastically scattered on a hydrogen nucleus, rather than on an oxygen nucleus, displayed in the right and left panels of Fig. 16, respectively.

References

- [1] <https://fluka.cern>, Accessed on: Sep. 23, 2024.
- [2] G. Battistoni, et al., Overview of the FLUKA code, *Ann. Nucl. Energy* 82 (2015) 10–18. doi:10.1016/j.anucene.2014.11.007.
- [3] C. Ahdida, et al., New Capabilities of the FLUKA Multi-Purpose Code, *Front. Phys.* 9, [Online]. Available: <https://www.frontiersin.org/journals/physics/articles/10.3389/fphy.2021.788253>. Accessed on: Sep. 20, 2024 (2022). doi:10.3389/fphy.2021.788253.
- [4] J. B. Potoine, et al., Power deposition studies for standard and crystal-assisted heavy ion collimation in the CERN Large Hadron Collider, *Phys. Rev. Accel. Beams* 26 (2023) 093001. doi:10.1103/PhysRevAccelBeams.26.093001.
- [5] D. Bozzato, et al., Advanced simulation techniques for Radiation Protection studies at the Large Hadron Collider, *Rad. Phys. Chem.* 218 (2024) 111573. doi:10.1016/j.radphyschem.2024.111573.
- [6] P. Dyrz, et al., In-situ radiological classification and characterization methodology of activated cables in par-

$E_p = 225 \text{ MeV}$

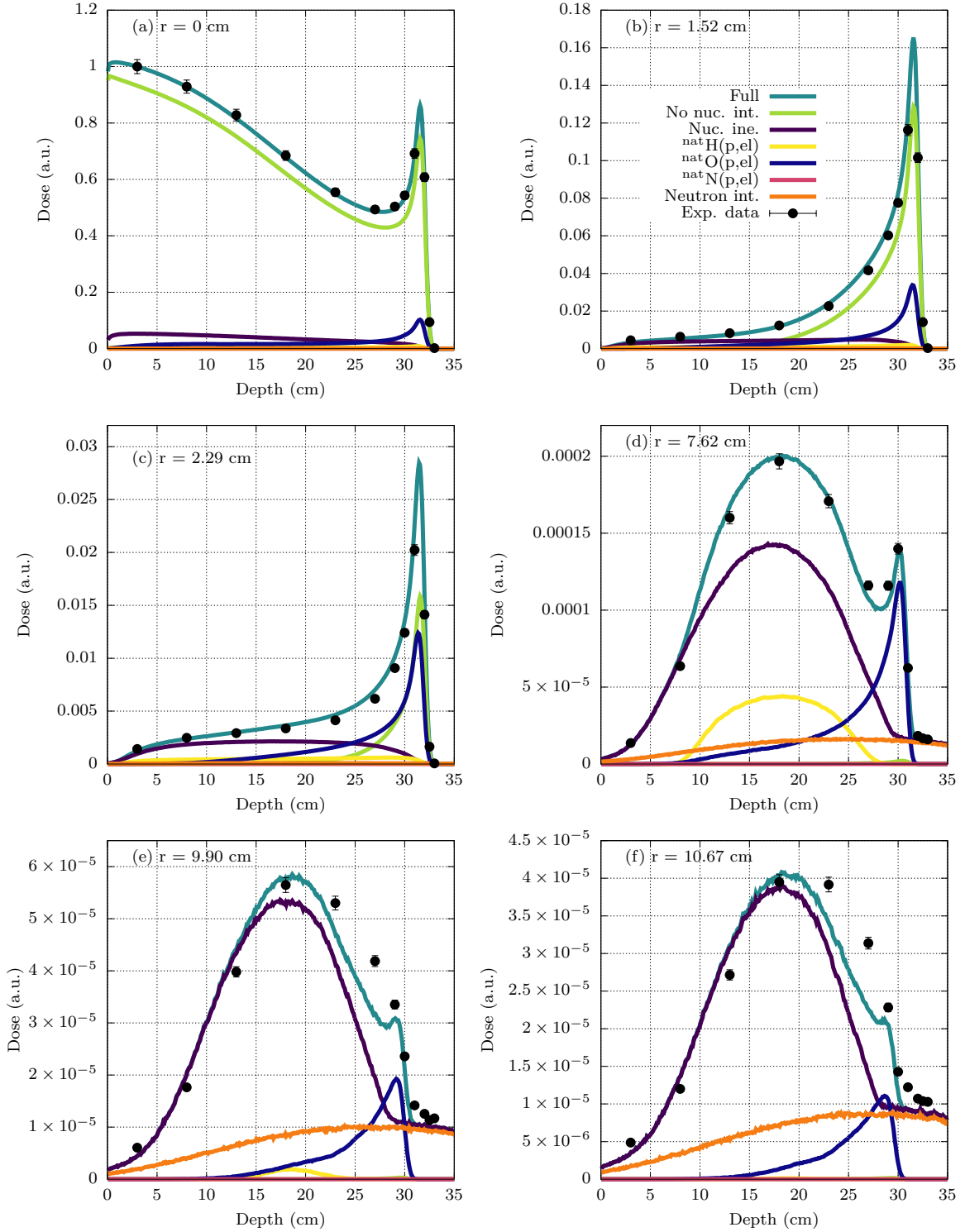


Figure 10: FLUKA v4-4.0 absorbed dose in arbitrary units as a function of depth by 225 MeV protons in water, resolved into the contribution of various kind of particle histories (see key and text).

$E_p = 160 \text{ MeV}$

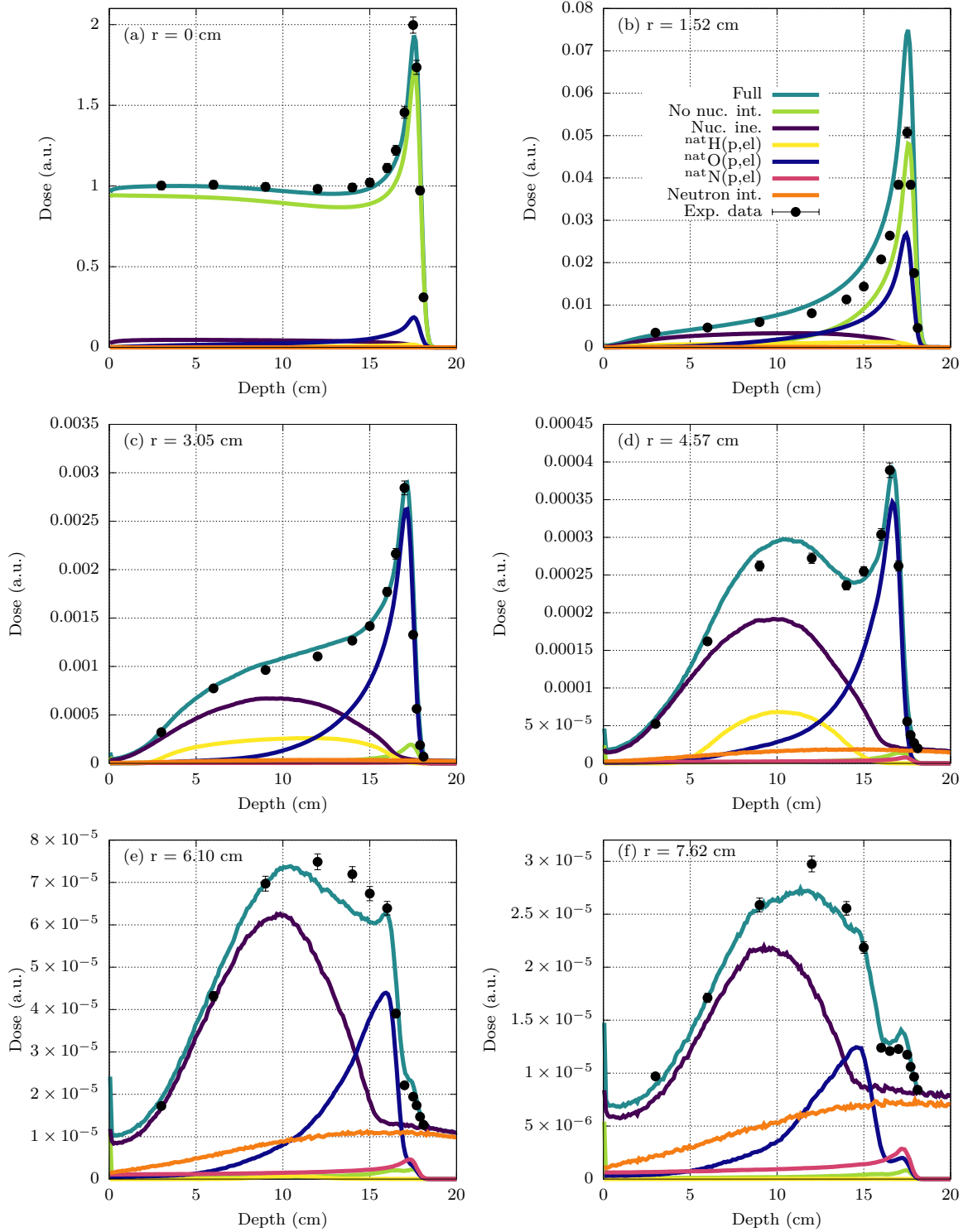


Figure 11: Same as Fig. 10 for 160 MeV protons.

$E_p = 100$ MeV

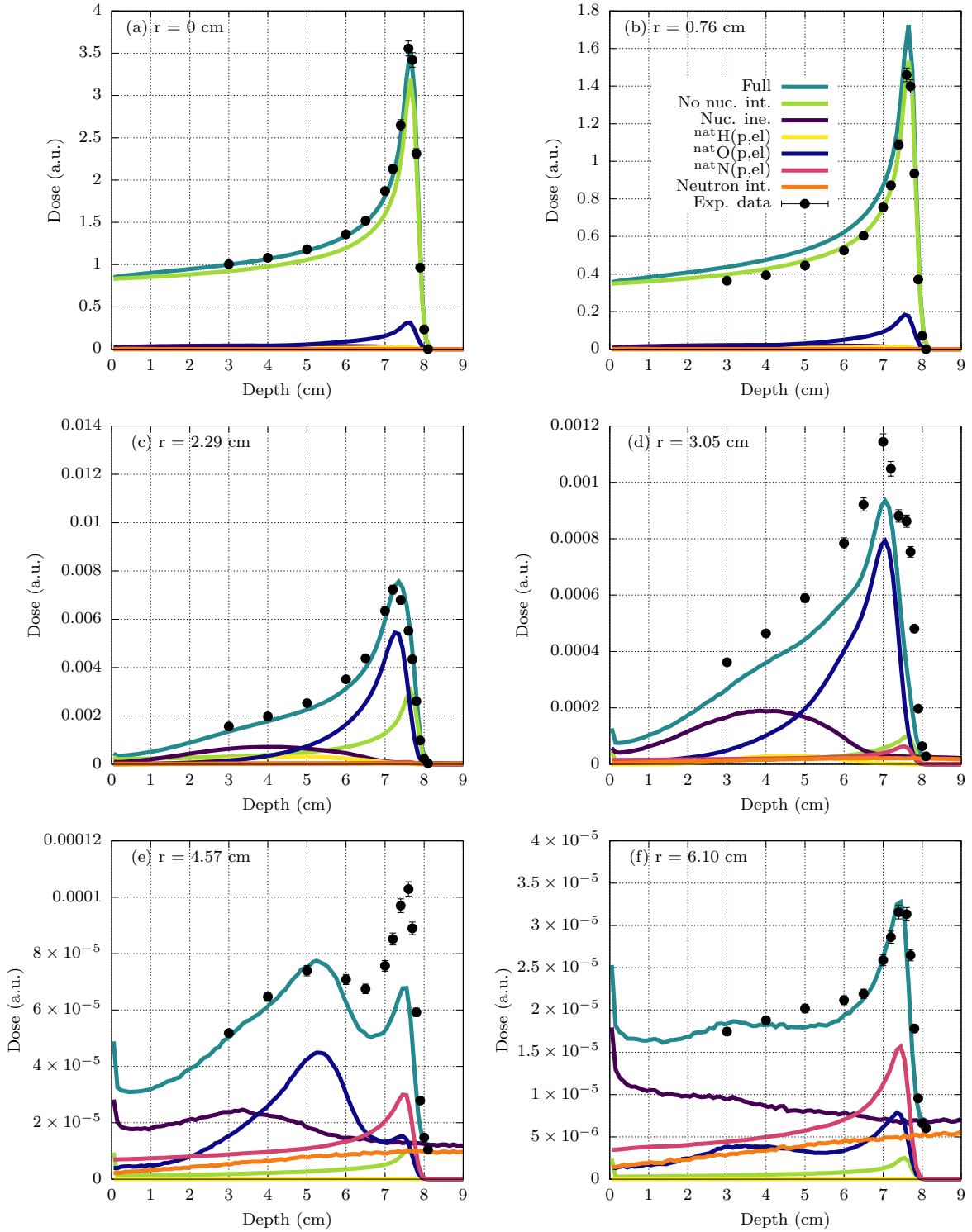


Figure 12: Same as Fig. 10 for 100 MeV protons.

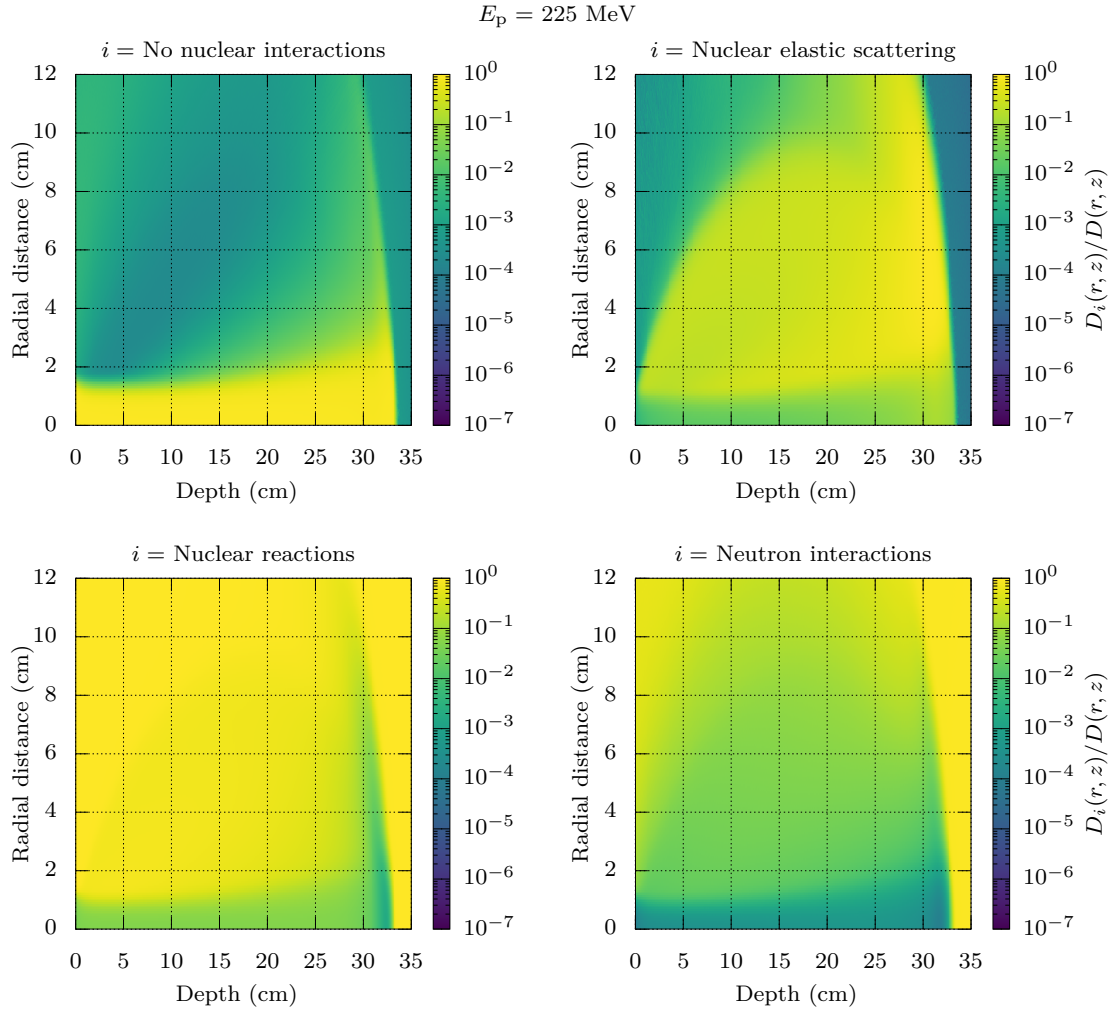


Figure 13: Ratio between the FLUKA v4-4.0 absorbed dose due to various interaction mechanisms (see key and text) and the total absorbed dose for 225 MeV protons in water.

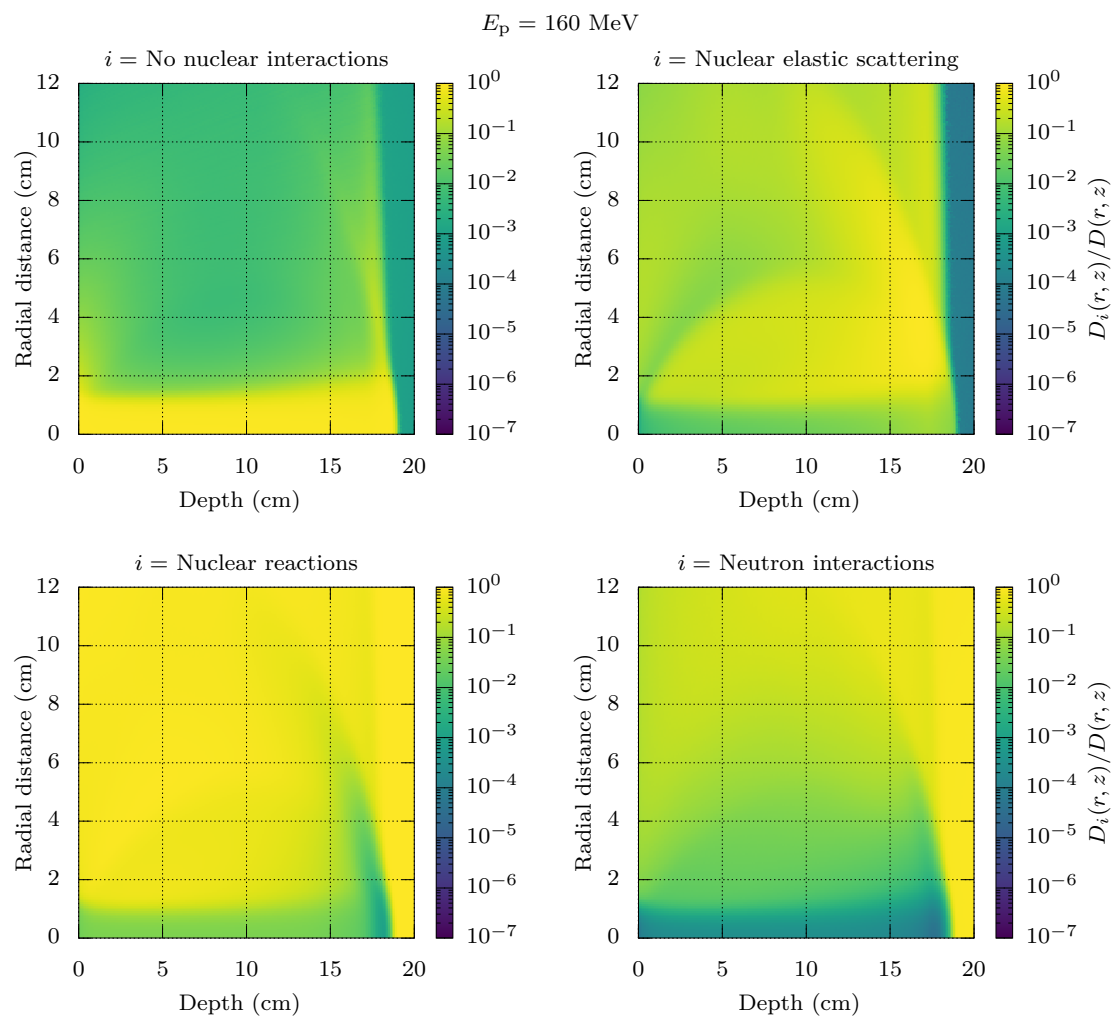


Figure 14: Same as Fig. 13 for 160 MeV protons.

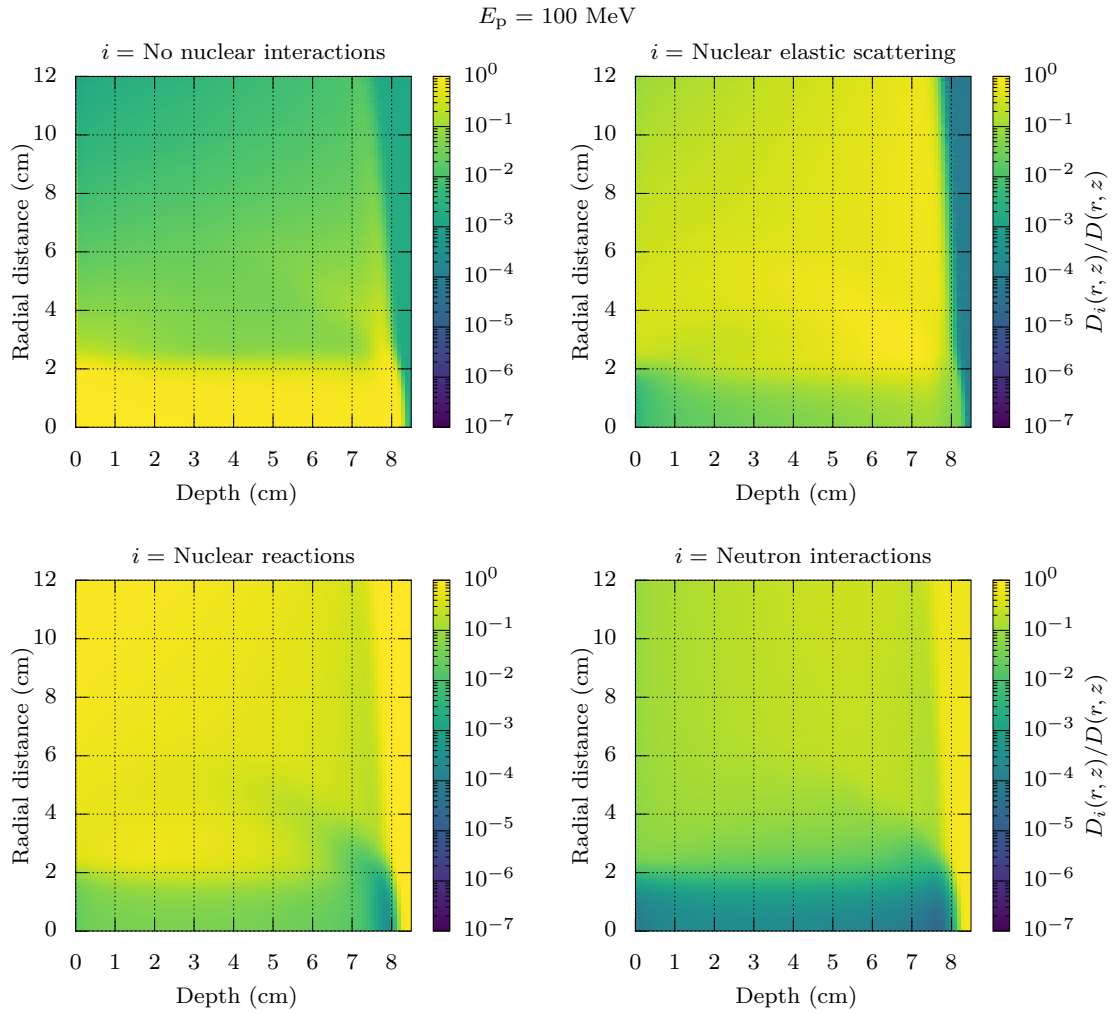


Figure 15: Same as Fig. 13 for 100 MeV protons.

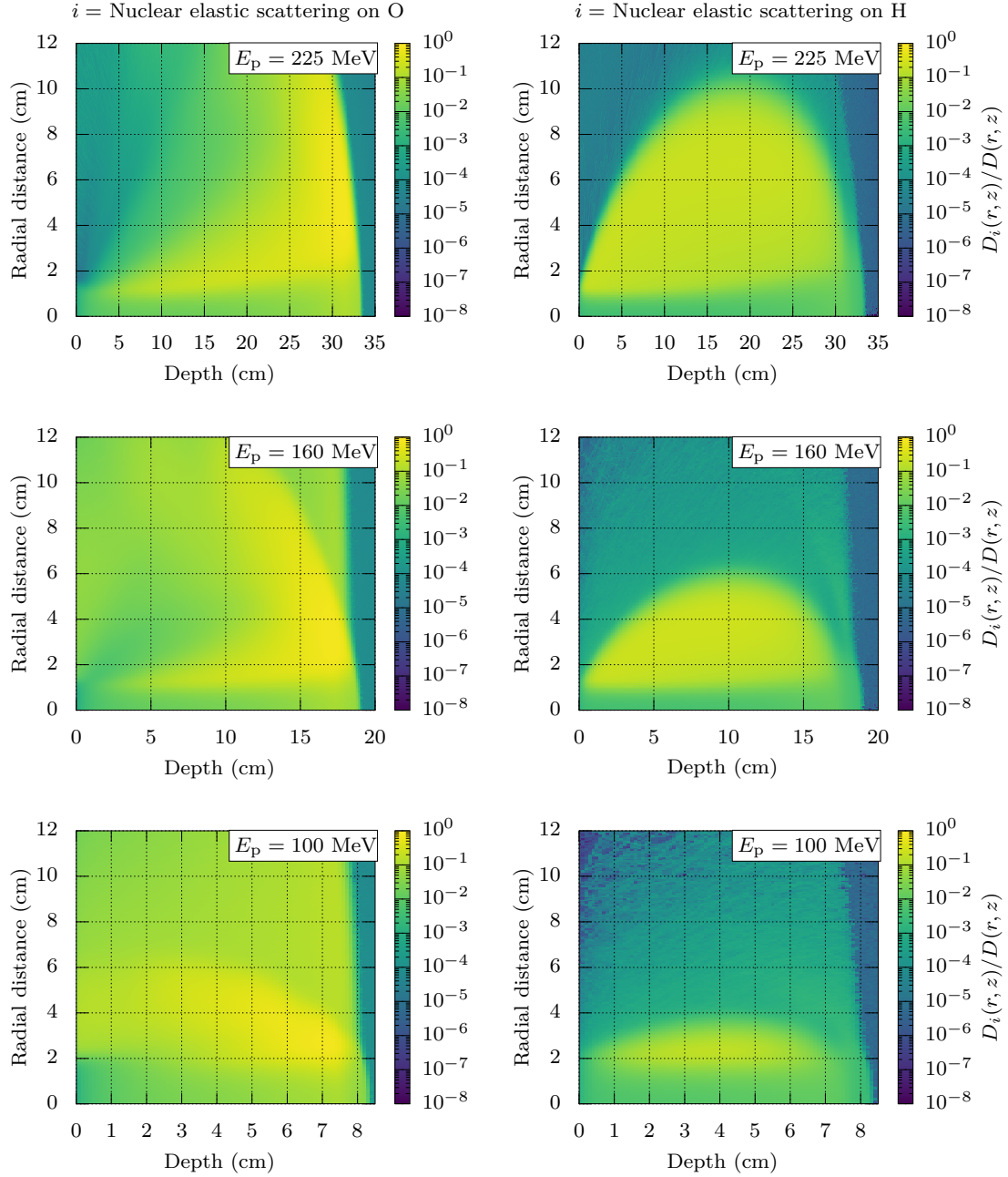


Figure 16: Ratio of the FLUKA v4-4.0 absorbed dose due to histories from nuclear elastic scattering of protons on oxygen (left panels) and hydrogen (right panels) to the total absorbed dose for 225 MeV, 160 MeV, and 100 MeV protons (first, second, and third row, respectively) in water.

- title accelerators, *Rad. Phys. Chem.* 216 (2024) 111439. doi:10.1016/j.radphyschem.2023.111439.
- [7] G. Lerner, et al., Analysis of the Photoneutron Field Near the THz Dump of the CLEAR Accelerator at CERN With SEU Measurements and Simulation, *IEEE Trans. Nucl. Sci.* 69 (7) (2022) 1541–1548. doi:10.1109/TNS.2022.3157404.
- [8] G. Lerner, et al., Analysis of the Radiation Field Generated by 200-MeV Electrons on a Target at the CLEAR Accelerator at CERN, *IEEE Trans. Nucl. Sci.* 70 (8) (2023) 1572–1579. doi:10.1109/TNS.2023.3252808.
- [9] M. Cecchetto, et al., 0.1-10 MeV Neutron Soft Error Rate in Accelerator and Atmospheric Environments, *IEEE Trans. Nucl. Sci.* 68 (5) (2021) 873–883. doi:10.1109/TNS.2021.3064666.
- [10] E. Ramoisiaux, et al., Ambient dose simulation of the ProtherWal proton therapy centre radioactive shielding decay using BDSIM and FISPACT-II, *EPJ Nuclear Sci. Technol.* 9 (2023) 27. doi:10.1051/epjn/2023011.
- [11] C. Hernalsteens, et al., A hybrid numerical approach to the propagation of charged particle beams through matter for hadron therapy beamline simulations, *Nucl. Instrum. Meth. B* 531 (2022) 56–64. doi:10.1016/j.nimb.2022.09.005.
- [12] A. Hadadi, S. Ghanavati, ^{75}Se - A promising alternative to ^{192}Ir for potential use in the skin cancer brachytherapy: A Monte Carlo simulation study using FLUKA code, *Appl. Radiat. Isot.* 197 (2023) 110786. doi:10.1016/j.apradiso.2023.110786.
- [13] A. Coronetti, et al., Assessment of Proton Direct Ionization for the Radiation Hardness Assurance of Deep Submicron SRAMs Used in Space Applications, *IEEE Trans. Nucl. Sci.* 68 (5) (2021) 937–948. doi:10.1109/TNS.2021.3061209.
- [14] J. Ranft, Estimation of radiation problems around high-energy accelerators using calculations of the hadronic cascade in matter, *Part. Accel.* 3 (1972) 129–161.
- [15] A.-G. Şerban, A. Coronetti, R. García Alía, F. Salvat Pujol, Nuclear elastic scattering of protons below 250 MeV in FLUKA v4-4.0 and its role in single-event-upset production in electronics, *Comp. Phys. Comm.* (2024) 109276.
- [16] N. Otuka, et al., Towards a More Complete and Accurate Experimental Nuclear Reaction Data Library (EXFOR): International Collaboration Between Nuclear Reaction Data Centres (NRDC), *Nucl. Data Sheets* 120 (2014) 272–276. doi:10.1016/j.jnds201407065.
- [17] V. Zerkin, B. Pritychenko, The experimental nuclear reaction data (EXFOR): Extended computer database and Web retrieval system, *Nucl. Instrum. Meth. A* 888 (2018) 31–43. doi:10.1016/j.nima.2018.01.045.
- [18] A.-G. Şerban, A. Coronetti, R. García Alía, F. Salvat Pujol, RPP-model trends across technology nodes for the MC simulation of SEUs in commercial SRAMs under proton irradiation, *IEEE Trans. Nucl. Sci.* (2024). doi:10.1109/TNS.2024.3520506.
- [19] A. Akkerman, J. Barak, N. Yitzhak, Role of Elastic Scattering of Protons, Muons, and Electrons in Inducing Single-Event Upsets, *IEEE Trans. Nucl. Sci.* 64 (10) (2017) 2648–2660. doi:10.1109/TNS.2017.2747658.
- [20] P. Caron, et al., Physical Mechanisms of Proton-Induced Single-Event Upset in Integrated Memory Devices, *IEEE Trans. Nucl. Sci.* 66 (7) (2019) 1404–1409. doi:10.1109/TNS.2019.2902758.
- [21] J. Mott, J. Daniel, Interactions of Electromagnetic Radiation and Subatomic Particles with Matter - Part 2, *Clin. Oncol.* 33 (7) (2021) 455–460. doi:10.1016/j.clon.2021.02.005.
- [22] N. Verbeek, et al., Single pencil beam benchmark of a module for Monte Carlo simulation of proton transport in the PENELOPE code, *Med. Phys.* 48 (1) (2021). doi:10.1002/mp.14598.
- [23] L. Eyges, Multiple Scattering with Energy Loss, *Phys. Rev.* 74 (1948) 1534–1535. doi:10.1103/PhysRev.74.1534.
- [24] B. Rossi, K. Greisen, Cosmic-Ray theory, *Rev. Mod. Phys.* 12 (1941) 240–309. doi:10.1103/RevModPhys.12.240.
- [25] B. Gottschalk, Techniques of Proton Radiotherapy: Transport Theory, <https://arxiv.org/abs/1204.4470> (2012).
- [26] V. Vlachoudis, FLAIR: A Powerful But User Friendly Graphical Interface For FLUKA, in: *Proc. Int. Conf. on Mathematics, Computational Methods & Reactor Physics*, Saratoga Springs, New York, USA, 2009.
- [27] A. Donadon, G. Hugo, C. Theis, V. Vlachoudis, FLAIR3 – recasting simulation experiences with the Advanced Interface for FLUKA and other Monte Carlo codes, *EPJ Web Conf.* 302 (2024) 11005. doi:10.1051/epjconf/202430211005.
- [28] M. Berger, J. Coursey, M. Zucker, ESTAR, PSTAR, and ASTAR: Computer Programs for Calculating Stopping-Power and Range Tables for Electrons, Protons, and Helium Ions (version 1.21), <http://physics.nist.gov/Star>, accessed: September 12, 2024 (1999).
- [29] <https://physics.nist.gov/PhysRefData/Star/Text/ESTAR.html>, accessed: October 3, 2024.
- [30] S. Seltzer, et al., Key data for ionizing-radiation dosimetry: measurement standards and applications, *ICRU Report* 90 (2016).
- [31] B. Gottschalk, E. Cascio, J. Daartz, M. Wagner, On the nuclear halo of a proton pencil beam stopping in water, *Phys. Med. Biol.* 60(14) (2015) 5627–5654. doi:10.1088/0031-9155/60/14/5627.
- [32] R. Zhang, P. Taddei, M. Fitzek, W. Newhauser, Water equivalent thickness values of materials used in beams of protons, helium, carbon and iron ions, *Phys. Med. Biol.* 55 (2010) 2481. doi:10.1088/0031-9155/55/9/004.
- [33] A. Burin, I. Branco, H. Yoriyaz, Determination of WER and WET equivalence estimator for proton beams in the therapeutic energy range using MCNP6.1 and TOPAS codes, *Rad. Phys. Chem.* 203 (2023) 110606. doi:10.1016/j.radphyschem.2022.110606.
- [34] T. Bortfeld, An analytical approximation of the Bragg curve for therapeutic proton beams, *Med. Phys.* 24(12) (1997) 2024–2033. doi:10.1118/1.598116.
- [35] <https://physics.nist.gov/PhysRefData/Star/Text/PSTAR.html>, accessed: September 12, 2024.